sustainability

MDPI

Article

Mechanical Properties and Energy Characteristics of Flawed Samples with Two Non-Parallel Flaws under Uniaxial Compression

Qun Li [1], Changfu Huang [2], Yanbo Zhang [1], Peng Liang [1,*], Xulong Yao [1] and Guangyuan Yu [1]

[1] College of Mining Engineering, North China University of Science and Technology, Tangshan 063210, China
[2] China Railway 15th Bureau Group Co., Ltd., Shanghai 200070, China
* Correspondence: hnlp87@163.com

Abstract: Unequal flaws are widespread in rock engineering, in which the extensions induced by excavation and unloading are the main factors leading to engineering instability. Rock deformation and failure are essentially the results of energy transmission. In order to study the influence of flaw type and angle on the mechanical properties and energy characteristics of the flawed rock mass, uniaxial compression tests were conducted using particle flow numerical analysis software. The results show that the crack initiation strength and peak strength of the sample increase with the increase in the flaw angle. For smaller flaw angles, the sample shows obvious plastic deformation during uniaxial compression. For larger flaw angles, the sample shows elastic–brittle properties, whose storage energy is larger. The peak strength of samples with flaws of unequal length presents an obvious decrease compared with that of flawed samples with flaws of equal length, and the extent of the reduction is 6.15% on average. Unequal flaws decrease the ability of the flawed sample to absorb strain energy. Compared with flawed samples with equal flaws, flawed samples with unequal flaws decrease the boundary energy and elastic strain energy by 9.29% and 9.95% on average, respectively. Flaws of unequal length in this sample can weaken the performance of the flawed sample.

Keywords: rock mechanics; flawed rock mass; non-parallel flaws; energy characteristics

Citation: Li, Q.; Huang, C.; Zhang, Y.; Liang, P.; Yao, X.; Yu, G. Mechanical Properties and Energy Characteristics of Flawed Samples with Two Non-Parallel Flaws under Uniaxial Compression. *Sustainability* **2023**, *15*, 459. https://doi.org/10.3390/su15010459

Academic Editors: Fan Feng, Eryu Wang and Ruifeng Huang

Received: 17 November 2022
Revised: 19 December 2022
Accepted: 22 December 2022
Published: 27 December 2022

1. Introduction

Rock masses contain many micro-cracks or flaws that are randomly distributed and are observed at different scales [1,2]. These defects can easily cause the initiation, propagation, and coalescence of cracks under the action of external loads, which greatly affects the strength of the rock mass, leading to the failure or deformation of the rock masses. Therefore, it is vital to study the mechanical properties and crack propagation characteristics of flawed rock masses.

Many scholars have carried out related research on flawed rock masses. Bobet [3] and Park [4,5] studied the compression process of flawed rock and systematically analyzed the propagation and failure mode of wing cracks and secondary cracks. Wong and Chau [6] and Wong and Einstein [7] studied the crack-propagation and coalescence behavior of Carrara marble specimens containing two pre-existing parallel flaws on the macro and micro scales. Morgan et al. comprehensively studied the cracking and coalescence behavior of granite specimens with pre-existing flaws and determined the mode of cracking (tensile or shear) [8]. Lee and Jeon [9] investigated non-parallel flaws on three kinds of materials (PMMA, Diastone, and Hwangdeung granite) and analyzed the influence of the flaw angle on crack initiation. Yang et al. [10] investigated the strength failure and crack-coalescence behavior of red sandstone containing two unparallel flaws experimentally. Afolagboye et al. [11] investigated the cracking behavior and coalescence process in a brittle material with two non-parallel flaws and analyzed the influence of crack angle and rock bridge length on cracks' initiation position and propagation path. Meanwhile,

other scholars have also carried out relevant research on the mechanical properties, crack propagation, and coalescence behavior of flawed rock masses [12–17].

Rock deformation and failure are essentially the results of energy transmission. Some scholars have studied the evolution of energy under cracks' inclination angles. Huang and Cen [18] used a particle flow code (PFC) to study the energy dissipation mechanism of rock specimens with a single flaw under uniaxial compression. The more dissipated the energy and stored elastic strain energy at peak strength are, the stronger the damage flaw at the post-peak is with the increase in flaw angle. Jin et al. [19] studied the influence of flaw angle on the energy mechanism of a rock-like sample with a single flaw by using PFC. The input energy, strain energy, and dissipated energy of a specimen showed approximate increasing trends as the flaw angle increased. Li et al. [20] explored the influence of flaw angle on the mechanical properties and energy evolution of sandstone under uniaxial loading tests. They pointed out that the elastic energy, dissipated energy, and input energy at the peak point of flawed sandstone always decreased with the increase in the flaw angle.

Although the studies described above conducted in-depth research on various flawed rock, the research is mainly focused on flawed rocks of equal length. In practical engineering, the flawed rock masses are random flaw systems, and the flaws are generally unequal in length. Wang et al. [21] conducted mechanical tests on rock-like samples with two unequal flaws and pointed out that the propagation and coalescence of secondary cracks are affected by the main crack. Craciun et al. [22] determined the critical values of the incremental stress at which the crack tips begin to propagate. The interaction of cracks with different lengths was analyzed with the change in flaw length and distance. Fan et al. [23] established the analytical formula for stress-intensity factors (SIFs) for an infinite plane containing two unequal collinear cracks. They showed that the SIFs at long crack tips are always larger than those at short crack tips. Yu et al. [24] performed a compression test of a cement specimen containing two unequal flaws and analyzed the effect of flaw distance on flaw interaction.

Most of the above research studies are focused on the rock-failure law and the crack propagation law. However, the evolution of rock deformation and failure is essentially a comprehensive result of energy dissipation and release [25]. There are few studies on the energy dissipation and release of flawed rock with flaws of unequal length. The purpose of the present paper is to analyze the influence of flaws of unequal length on rock mechanical properties and energy dissipation. Therefore, the remainder of this paper is organized as follows. In Section 2, a brief introduction to the experimental method and the simulation method for a parallel bond is provided. In Section 3, the effects of the flaw's inclination angle on the strength of the rock mass and crack characteristics are identified. In Section 4, the effect of flaw angle and the type on energy dissipation and the evolution process of energy are analyzed.

2. Establishment of the Calculation Model

2.1. Parallel Bond Model (PBM)

A parallel bond can be assumed to be a set of elastic springs with constant normal and shear stiffness. The elastic springs are uniformly distributed on the contact plane and centered on the contact point. When the parallel bond is created, a force and moment can be developed in the bond material at the contact point. The force and moment act on the two contacting pieces. They may be related to the maximum normal and shear stresses in the bond material. If any one of these maximum stresses exceeds its corresponding bond strength, the parallel bond is broken. The bond material is removed from the model along with its accompanying force, moment, and stiffness. The behavior of the parallel bond model with inactive dashpots can be seen in Figure 1.

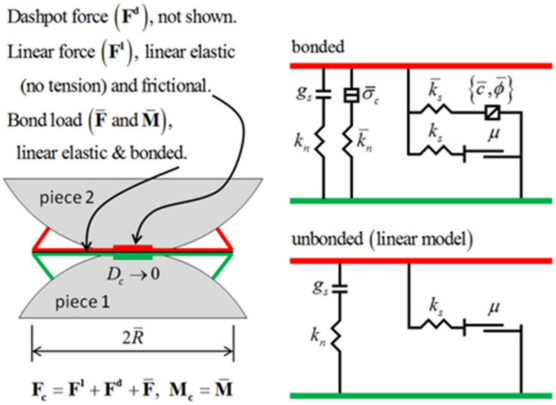

Figure 1. The behavior of the parallel bond model [26].

The parallel bond model (PBM) provides the behavior of two interfaces. ① The first interface is an infinitesimal linear elastic interface, which is equivalent to the linear model. The interface can only transmit force (dashpot force F^d, linear force F^l, and parallel-bond force $\overline{F}$) and does not resist the parallel-bond moment $\overline{M}$. ② The second interface is a finite-size and bonded interface, which can transmit the force and moment. When the second interface is bonded, it resists relative rotation. Its behavior is linear elastic until the strength limit is exceeded and the bond breaks (i.e., it is unbonded). When the second interface is unbonded, it does not carry any load. The unbonded linear parallel bond model is equivalent to the linear model.

The failure envelope for the parallel bond is shown in Figure 2 ($\overline{\tau_c}$ is the shear strength, $\overline{\sigma_t}$ is the tensile strength). If the tension or shear strength limit is exceeded ($\overline{\sigma} > \overline{\sigma_t}$ or $\overline{\tau} > \overline{\tau_c}$), then the bond in the tension or shear is broken. The stress expression of the parallel bond model is given as follows:

$$\overline{\sigma} = \frac{\overline{F_n}}{\overline{A}} + \overline{\beta}\frac{\|\overline{\mathrm{M_b}}\|\overline{R}}{\overline{I}},\ \text{with}\ \overline{\beta} \in [0,1] \tag{1}$$

$$\overline{\tau} = \frac{\|\overline{F_s}\|}{\overline{A}} \tag{2}$$

where $\overline{F_n}$ and $\overline{F_s}$ is the normal force and shear force, respectively; $\overline{\mathrm{M_b}}$ is the parallel-bond moment; $\overline{A}$ is the cross-sectional area; $\overline{R}$ is the average radius of particle 1 and particle 2; $\overline{I}$ is the moment of inertia of the parallel bond cross-section, and $\overline{\beta}$ is the moment-contribution factor.

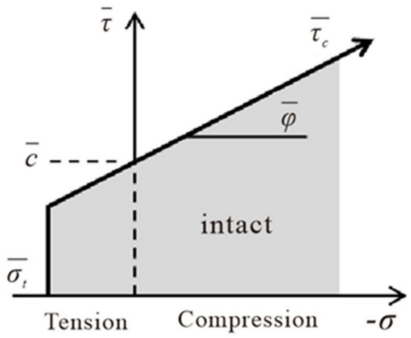

Figure 2. Failure envelop for the parallel bond [26].

2.2. Numerical Model Description and Calibration of the PBM

The numerical simulation in this paper is a further study based on a physical experiment by Afolagboye et al. [11]. Compared with the physical experiment, the numerical models were set to the same dimension as the physical sample, 152 mm × 76 mm. For the

sample with the open flaws of equal length, the length size of the flaw was 12.7 mm, as shown in Figure 3a. For the sample with the open flaws of unequal length, the lengths of the flaws are 20 mm and 12.7 mm, as shown in Figure 3b. The length of the rock bridge d under the two conditions is 12.7 mm, and the flaw angle θ is 30°, 45°, and 60°, respectively. Considering the flaw size and computational efficiency in the uniaxial compression test, the numerical models contain 29,400 grains. The same random seed was selected for the numerical simulation experiment to reduce the influence of uncertain factors. The grain diameter matched a Gaussian distribution with a minimum diameter equal to 0.55 mm and a maximum diameter equal to 0.80 mm. The flaws were established by deleting a finite plane of grains in the model's center. The model grain density was set to 2200 kg/m^3 to match the actual material density.

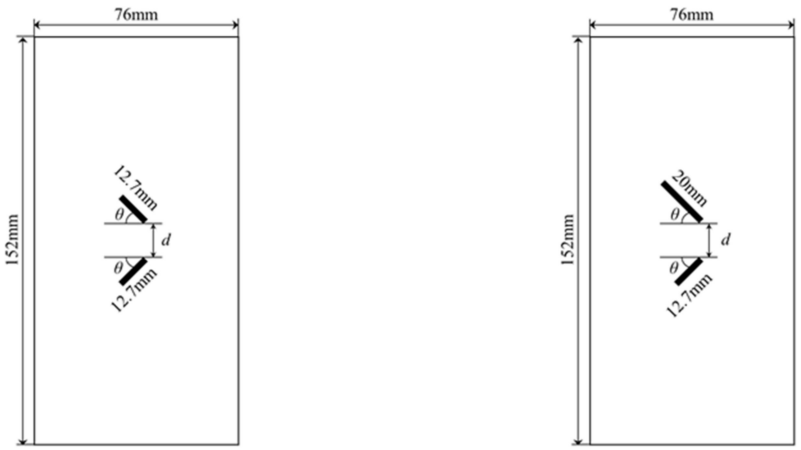

Figure 3. Schematic diagram of model size and flaw distribution: (**a**) Sample with flaws of equal length, and (**b**) Sample with flaws of unequal length.

In the numerical simulation, the axial compressive force was continuously applied to the top and bottom walls to shrink the numerical model. The sample was loaded vertically in a constant servo-control manner until failure. In order to ensure the quasi-static equilibrium of the sample in each step, a sufficiently slow loading speed was used in the simulation, i.e., 0.025 m/s [27]. The compression test was fully unconfined until the axial compressive force dropped to 80% of the peak strength.

The numerical model was calibrated by adjusting the model parameters via the methods suggested by Potyondy [28] and Zhang [29]. The particle diameters satisfied a Gaussian distribution bounded by $d_{\min}$ and $d_{\max}$. The grain diameter matched a minimum diameter equal to 0.55 mm and a maximum diameter equal to 0.80 mm. The effective modulus of both the particle and the bond is directly proportional to the stiffnesses of the particle (k_n, k_s) and those of the parallel bond $\left(\overline{k_n}, \overline{k_s}\right)$, respectively. The effective modulus (E_c, $\overline{E_c}$) was chosen to match the Young modulus. The radius multiplier parameter λ was used to set the parallel bond radius $R = \lambda \min(R_A, R_B)$. R_A and R_B are the radii of any two neighboring particles. The ratio of the parallel bond cohesion strength $\overline{c}$ and parallel bond tensile strength $\overline{\sigma_c}$ is a dominant parameter in determining the mode of bond breakage. When $\overline{\sigma_c}/\overline{c} = 0.71$, the numerical results are consistent with the comparative experiments. When the macro mechanical behavior of numerical simulation is basically consistent with that of the physical experiment, the proper microparameters applied to generate the PBM are obtained, which are listed in Table 1. The mechanical characteristics and crack-propagation paths obtained from the physical test and numerical simulation are shown in Tables 2 and 3.

Table 1. Microparameters of the PBM used to simulate the behavior of the sample.

Microparameter	Value
Minimum grain diameter, $d_{\min}$(mm)	0.55
Maximum to minimum grain diameter ratio, $d_{\max}/d_{\min}$	1.45
Installation gap, g_{gap}	0.53×10^{-4}
Effective modulus of both particle and bond, $E_c = \overline{E_c}$ (GPa)	4.7
Ratio of normal to shear stiffness of both particle and parallel bond, $k_n/k_s = \overline{k_n}/\overline{k_s}$	1.5
Radius multiplier parameter, λ	1.0
Mean and standard deviation bond parallel bond tensile strength, $\overline{\sigma_c}$ (MPa)	23.0
Mean and standard deviation bond parallel bond cohesion strength $\overline{c}$ (MPa)	32.5

Table 2. Comparison of experimental and simulation parameters.

Type	Density/(kg/m^3)	Young Modulus/GPa	UCS/MPa
Experimental data	2200	7.50	46.35
Simulated data	2200	7.54	46.10

Table 3. Comparison of crack-propagation paths between physical experiments and numerical simulation experiments.

Flaw Angle θ/(°)	Schematic Diagram of Experimental Crack Propagation	Simulated Diagram
30	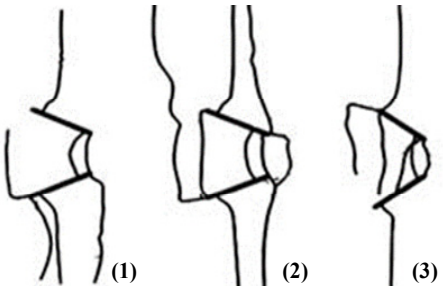	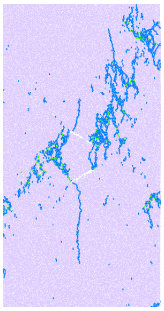
45	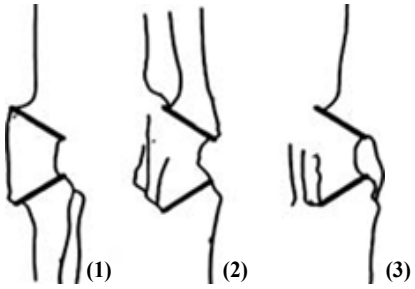	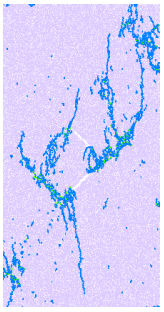
60	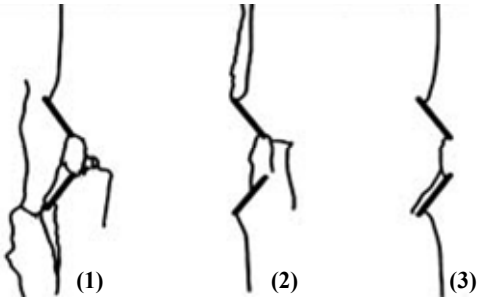	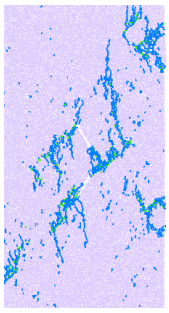

3. Numerical Experiment Results

3.1. Stress–Strain Curve Characteristics

The diagram of the axial stress–strain curves under different flaw angles can be seen in Figure 4. Sample E is composed of E30, E45, and E60. E30, E45, and E60 represent samples with flaws of equal length under the conditions of flaw angles θ of 30°, 45°, and 60°, respectively. F30, F45, and F60 are included in Sample F. F30, F45, and F60 represent samples with flaws of unequal length under the conditions of flaw angles θ of 30°,45°, and 60°, respectively.

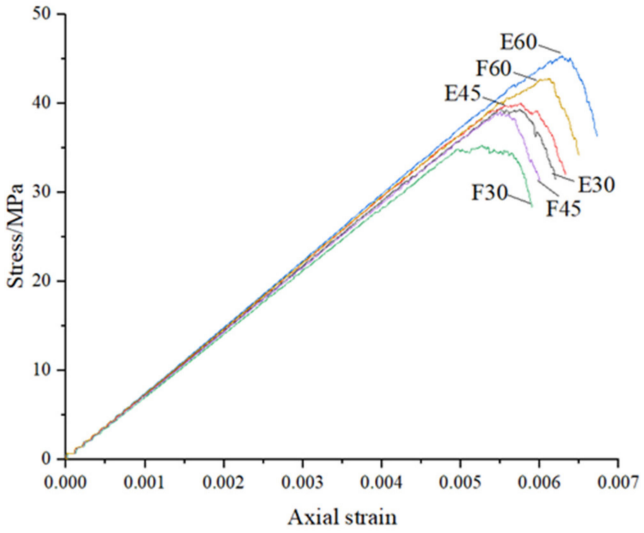

Figure 4. Axial stress–strain curves for different samples.

As shown in Figure 4, there is an obvious linear stage in the stress–strain curve for samples E and F. The plastic deformation stage appears before the peak stress, showing a stage characteristic. The stress growth rate of the sample decreases with the increase in axial strain. The stress drops rapidly after the peak of the curve, and the samples show the obvious characteristics of the brittle material.

The variation in elastic modulus with flaw angle is shown in Figure 5. For samples E and F, the samples with a larger flaw angle had a higher elastic modulus. When the flaw angle increased from 30° to 60°, the elastic modulus increased by 3.45% on average. The elastic modulus was reduced owing to the presence of the flaws of unequal length. The elastic modulus for Sample E was 13.74% on average higher than that for Sample F.

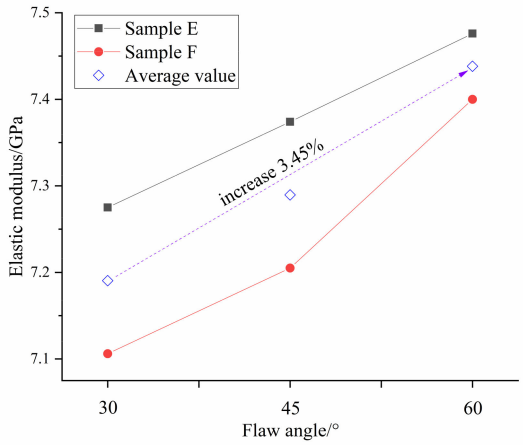

Figure 5. Variation in elastic modulus of a sample with different flaw angles.

3.2. Strength and Crack Characteristics

The axial stress–strain curve and crack number diagram under different flaw angles can be seen in Figure 6. The strength characteristics of different flawed samples are listed in Table 4.

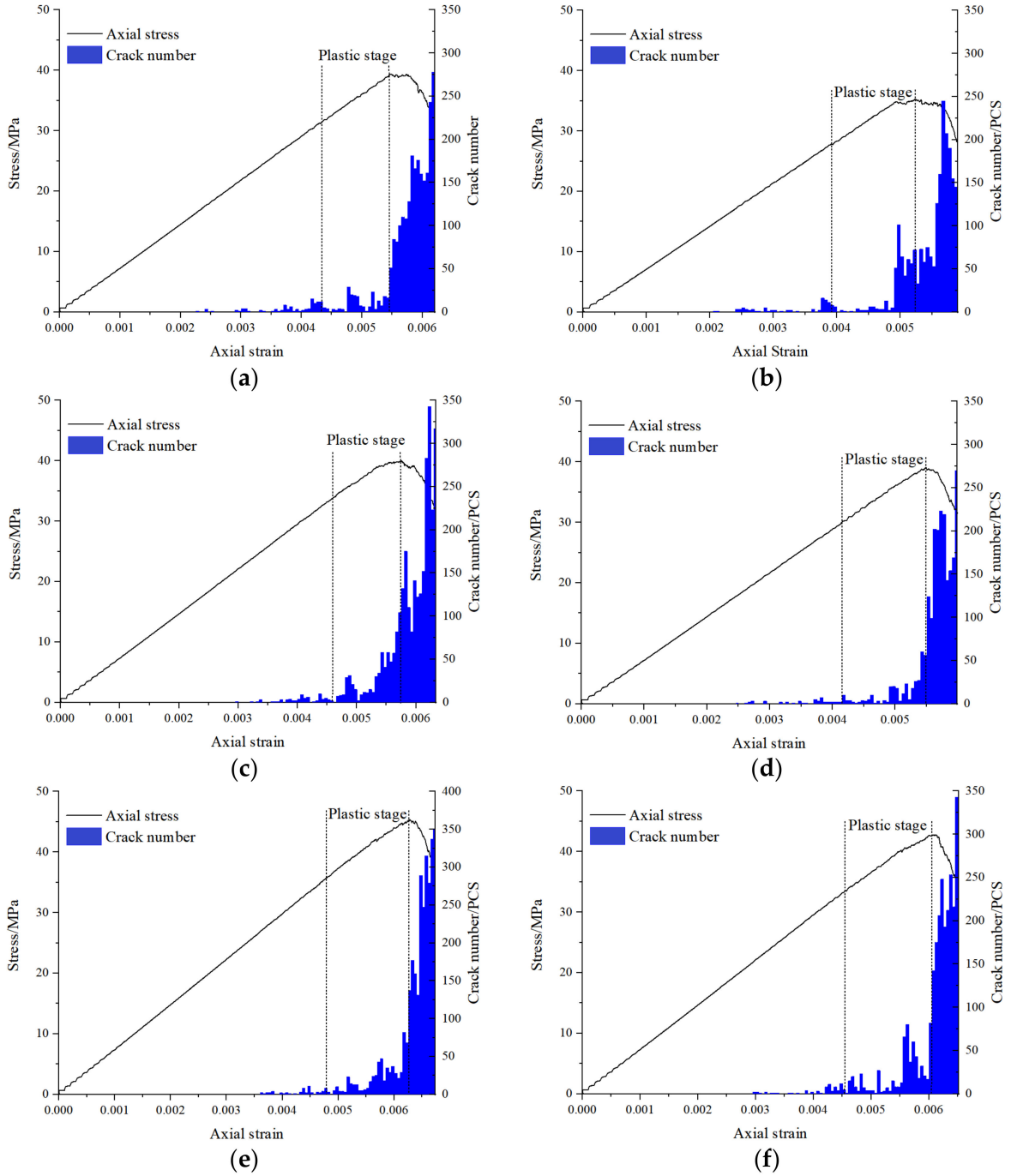

Figure 6. Axial stress–strain curve and crack number diagram under different flaw angles: (**a**) E30; (**b**) F30; (**c**) E45; (**d**) F45; (**e**) E60; and (**f**) F60.

Table 4. Strength characteristics of different flawed samples.

Flaw Angle/(°)	Sample E (Equal Length Flaws)		Sample F (Flaws of Unequal Length)	
	Crack Initiation Strength /MPa	Peak Strength/MPa	Crack Initiation Strength/MPa	Peak Strength/MPa
30	18.55	39.37	15.31	35.27
45	22.15	39.98	18.02	39.03
60	27.22	45.35	21.73	42.78

In Figure 6, the crack number is relatively small before the plastic stage, which is less than 5% of the maximum value of the crack number. In the plastic stage, a large number of cracks were gradually generated. The internal damage of the sample was intensified, and the crack propagation accelerated. In the post-peak region of the stress–strain curve, the maximum number of cracks was reached. The crack number of the samples with different flaw types was concentrated in the plastic stage, and the number increased sharply after the peak point. It is shown that the penetration and friction slip of macro cracks in the post-peak stage led to a sharp increase in the number of cracks.

For the same flaw type (flaws of equal length or flaws of unequal length), the number of cracks increases with the increase in flaw angle in the post-peak region. The crack number of samples with an angle of 60° increases by approximately 30% compared with that of samples with an angle of 30°. Under the same condition of flaw angle, the crack number in Sample E is 13.17% on average higher than that in Sample F.

The flaw angle had a great influence on the strength of the sample. For the same flaw type (flaws of equal length or flaws of unequal length), the crack-initiation strength and peak strength of the sample increased with the increase in the flaw angle. The samples with a flaw angle of 60° performed the best. The peak strengths of samples with a flaw angle of 60° in samples E and F were 15.19% and 21.29% bigger than those of samples with a flaw angle of 30°, respectively. The flaws with a large dip angle were more conducive to the stability of the sample.

The flaw type (flaws of equal length or flaws of unequal length) had a certain influence on the crack-initiation strength and peak strength of the sample. The performance of Sample E was better than that of Sample F. The crack-initiation strength and peak strength of Sample F were 18.76% and 6.15% lower than those of Sample E, respectively. For the flaw angle of 60°, the peak strengths of samples E and F were 45.35 MPa and 42.78 MPa. The peak strength of Sample F was reduced by 5.99% compared to Sample E. The flaws of unequal length have a negative effect on the stability of the sample.

4. Energy Characteristic Analysis

4.1. Energy Analysis Principle

The laws of thermodynamics indicate that energy conversion is essential to the process of the change in the physical properties of matter. The evolution of rock deformation and failure is essentially a comprehensive result of energy dissipation and release [25]. Strain energy, which is associated with elastic deformation, mainly induces rock damage and results in the deterioration of material properties and loss of strength. The dissipated energy, corresponding with the irreversible deterioration of the sample, is the intrinsic cause of the sudden failure of the rock. The above two energy parameters play significant roles in the deformation and failure process of flawed samples.

It is assumed that the process of deformation and failure of the rock sample is in a closed system without heat exchange. According to the first law of thermodynamics, the total energy U (boundary energy) can be expressed as follows:

$$U = U^e + U^d \tag{3}$$

where U^{d} and U^{e} indicate the dissipated energy and strain energy, respectively.

Simulating the uniaxial compression test in PFC software, the boundary energy U is the total work done by the upper and lower loading plates on the specimen. In the linear parallel bond model, strain energy U^e consists of particle strain energy E_k and bond strain energy $\overline{E}_k$. Dissipated energy is composed of particle friction energy, damping energy, kinetic energy, etc. Then, strain energy is expressed as follows:

$$U^e = E_k + \overline{E}_k \tag{4}$$

where $E_k = \frac{1}{2}\left(\frac{\left(F_n^l\right)^2}{k_n} + \frac{\left\|F_s^l\right\|^2}{k_s}\right)$ and $\overline{E}_k = \frac{1}{2}\left(\frac{\overline{F}_n^2}{\overline{k}_n \overline{A}} + \frac{\left\|\overline{F}_s\right\|^2}{\overline{k}_s \overline{A}} + \frac{\left\|\overline{M}\right\|^2}{\overline{k}_n \overline{I}}\right)$. F_n^l and F_s^l are the particle contact forces in the normal and shear directions, respectively, and k_n and k_s are the normal stiffness and shear stiffness of the particle contact force. $\overline{F}_n$ and $\overline{F}_s$ are the parallel–bond forces in the normal and shear directions, respectively. $\overline{k}_n$ and $\overline{k}_s$ are the corresponding stiffness of each parallel–bond force. $\overline{M}$ is the parallel–bond moment. $\overline{I}$ is the moment of inertia of the parallel bond cross-section. $\overline{A}$ is the cross-sectional area.

4.2. Evolution Process of Energy

In order to analyze the energy evolution law of the flawed sample, flawed samples with a flaw angle of 60° were chosen as examples. The energy evolution curves of samples with different flawed types (equal length flaws or not) during loading are shown in Figure 7. The evolution process of energy can be divided into four stages: (1) the initial compression stage; (2) the linear development stage of dissipated energy; (3) the unstable development stage of dissipated energy; and (4) the post-peak acceleration stage. The detailed description of each stage is as follows:

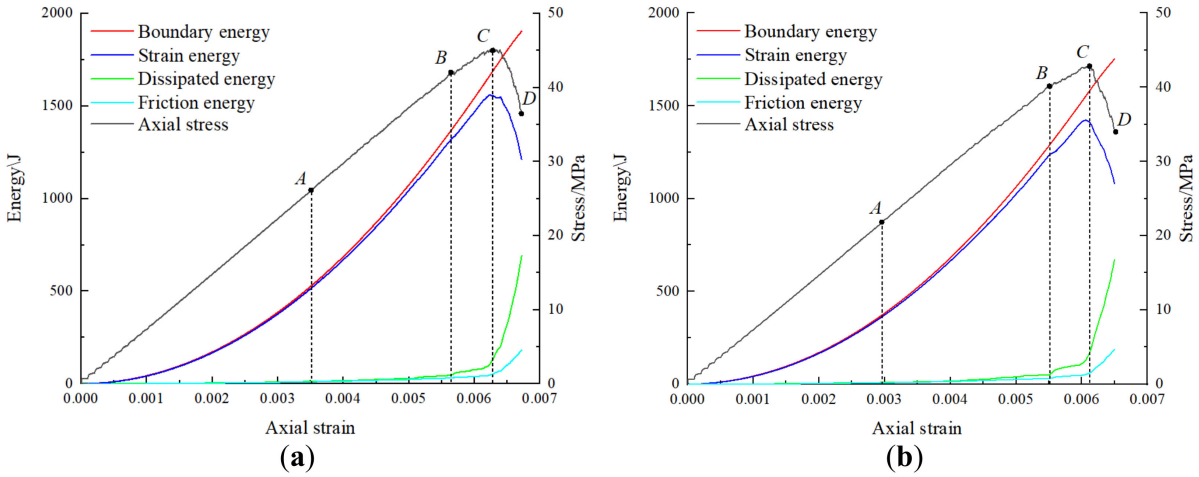

Figure 7. Energy evolution curve of flawed sample: (**a**) flaws of equal length; (**b**) flaws of unequal length.

(1) The initial compression stage (OA). From the beginning of the loading to point A, there is no crack in the sample. The boundary energy U, strain energy U^e, and dissipated energy U^d increase with the increase in axial strain, and the curves of U and U^e have a larger rate. At point A, the strain energy of samples with flaws of equal length and flaws of unequal length account for 97.66% and 97.58% of the boundary energy, respectively. The boundary energy is completely transformed into the strain energy of the sample. There is basically no energy dissipation. The dissipated energy and friction energy are almost zero.

(2) The linear development stage of dissipated energy (AB). The cracks begin to develop gradually after point A, but the growth rate is quite slow. In this stage, both the dissipated energy and friction energy increase linearly at a low rate. The curves of the boundary energy and strain energy grow approximately linearly. At point B, the

strain energy U^e of samples E and F account for 96.45% and 95.82% of the boundary energy U, respectively. Most of the energy is stored in the form of strain energy, which is energy accumulation.

(3) The unstable development stage of dissipated energy (*BC*). With the increase in axial stress, the cracks continue to develop and propagate, causing part of the strain energy to be released. The curve of the dissipated energy increases in a downward convex form, and the growth rate gradually becomes larger. Both the boundary energy and strain energy are increasing, but the slopes of the energy curves show a downward tendency. The two energy curves are clearly separated. At point *C*, the strain energy U^e reaches its maximum value, which is referred to as the energy storage limit of the sample.

(4) The post-peak acceleration stage (*CD*). At point *C*, the cracks propagate and coalesce into macroscopic cracks, and the strain energy curve begins to drop. The friction energy increases with the degree of friction slip of the cracks. It increases sharply at point *C* due to the penetration of macroscopic cracks. In the post-peak stage, the growth rate of boundary energy U shows a decreasing state. The strain energy U^e stored in the sample is gradually released and converted into dissipated energy such as friction energy. The dissipated energy of the sample increases exponentially. The proportion of the dissipated energy to the total energy gradually increases until the sample is destroyed.

Under the same flaw angle, the energy evolution process of the samples with flaws of equal length and flaws of unequal length is consistent. Before the peak strength, the energy is mainly stored in the form of strain energy. Only a small part of the energy, namely dissipated energy, is lost in the linear development stage (*AB*) and the unstable development stage (*BC*). In the post-peak stage, the released strain energy is transformed into dissipated energy, resulting in the overall failure of the sample. Specifically, compared with the sample with flaws of equal length, the peak strength and energy storage limit of samples with flaws of unequal length decrease to varying degrees.

4.3. Effect of Flaw Angle and Type on Energy Dissipation

Through the built-in fish language of the PFC, the internal energy evolution of the experimental system was monitored, and the boundary energy, strain energy, friction energy, and other energy could be obtained. Figure 8 shows the energy–strain curves of the samples with flaws of equal length and flaws of unequal length under different flaw angles. E30, E45, and E60 represent the curves of flaws of samples of equal length, respectively. F30, F45, and F60 represent curves of unequal-length flawed samples with 30°, 45°, and 60°, respectively.

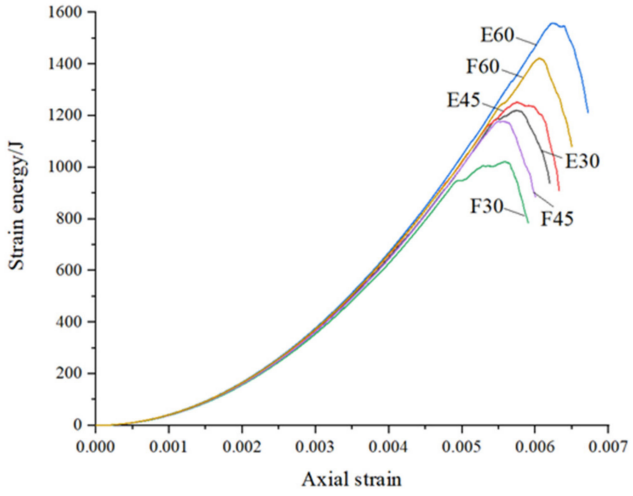

Figure 8. Strain energy–strain curves of samples.

As can be observed in Figure 8, the slopes of the six strain energy curves are basically the same when the axial strain is small ($\varepsilon < 0.004$). The strain energy was not affected by the flaw angle and length when $\varepsilon < 0.004$. For an axial strain $\varepsilon \geq 0.004$, the curves represent the separation trend, and the slopes of the six curves are different. Under the conditions of the same flaw type (equal flaws or unequal flaws), the strain energy of the sample with a flaw angle of 60° was greater than that of flawed samples with angles of 30° and 45°. The strain energy of the sample with a flaw angle of 30° was the smallest. Under the same flaw angle, the strain energy of the samples with flaws of equal length is significantly greater than that of the samples with flaws of unequal length. The existence of flaws of unequal length in the sample reduces the strain energy of the sample. Compared with equal length flawed sample, the unequal-length flawed sample is likely to be damaged.

Table 5 shows the boundary energy U, strain energy U^e, and dissipated energy U^d at the crack-initiation strength point and peak strength point in the deformation and failure process of flawed samples. It shows that whether the flaws are equal in length or not, the flaw angle and type affect the energy evolution characteristics of the samples. For the same flaw type, U and U^e at the crack initiation strength and peak strength increase with the increase in flaw angle. Samples E60 and F60 performed the best in samples E and F, respectively. For the same flaw angle, the values of U and U^e at the initiation strength and peak strength of the samples with flaws of equal length are greater than those of samples with flaws of unequal length. The lowest strain energy of the sample with flaws of equal length, U^e of 1187.86 J for Sample E30, is higher than that of Sample F30 (1003.29 J). The U^e of Sample E30 is 18.40% higher than that of Sample F30. The flaws of unequal length reduce the energy storage and release properties of the sample.

Table 5. Strength characteristics of different flawed samples.

Flaw Type	Sample No.	Flaw Angle/(°)	Crack Initiation Strength Point				Peak Strength Point			
			U/J	U^e/J	U^d/J	p_e/(%)	U/J	U^e/J	U^d/J	p_e/(%)
Equal length flaws (E)	E30	30	273.75	266.83	6.93	97.47	1259.45	1187.86	71.59	94.32
	E45	45	382.90	373.63	9.27	97.58	1401.88	1251.78	150.10	89.29
	E60	60	573.03	559.63	13.40	97.66	1690.57	1556.44	134.13	92.07
Flaws of unequal length (F)	F30	30	190.91	186.06	4.85	97.46	1123.51	1003.29	120.23	89.30
	F45	45	261.29	254.31	6.98	97.33	1256.99	1176.69	80.30	93.61
	F60	60	370.73	361.74	8.99	97.58	1567.06	1418.39	148.67	90.51

To further reveal the relationship between U^e and U, the strain energy ratio p_e was proposed by Li et al. [30], which can be obtained by using the following Equation:

$$p_e = \frac{U^e}{U} \times 100\% \quad (5)$$

The values of p_e at the crack-initiation strength point and peak strength point in the deformation and failure process of flawed samples can be seen in Table 5. The values of p_e at the crack initiation point are roughly the same. The flaw type and angle do not affect the strain energy ratio of the initiation strength. The ratio of the energy consumed by the crack initiation of a sample to the total energy is fixed. At the peak strength point, the values of p_e vary from 89.29% to 94.32% and are 91.52% on average. Whether the sample has flaws of equal length or not, the internal deformation and failure of the sample require only a small amount of external force to be applied. Due to the existence of a large amount of strain energy U^e, the stress is suddenly released during the uniaxial compression. Furthermore, the average value of p_e at the peak strength of the samples with flaws of unequal length is slightly smaller than that of the samples with flaws of equal length. Compared with the sample with flaws of equal length, less energy is taken to destroy the sample with flaws of unequal length.

The curves of the energy and crack number evolution of flawed samples can be seen in Figure 9. Under the same flaw type, as the flaw angle becomes larger, the total number of cracks at the final failure tends to increase. The total number of cracks in samples E60 and F60 is approximately twice that in samples E30 and F30, respectively. Dissipated energy is positively correlated with the number of cracks. The increase in crack propagation and coalescence is mainly caused by dissipated energy. Many cracks are generated after the peak strength point. The number of cracks before the peak strength is relatively small, accounting for 36.66% of the total number of cracks on average. Compared with Sample E, the number of cracks at the peak strength point of Sample F is large. The boundary energy U and the strain energy U^e of Sample F are small. This means that relatively little energy makes more cracks inside the sample.

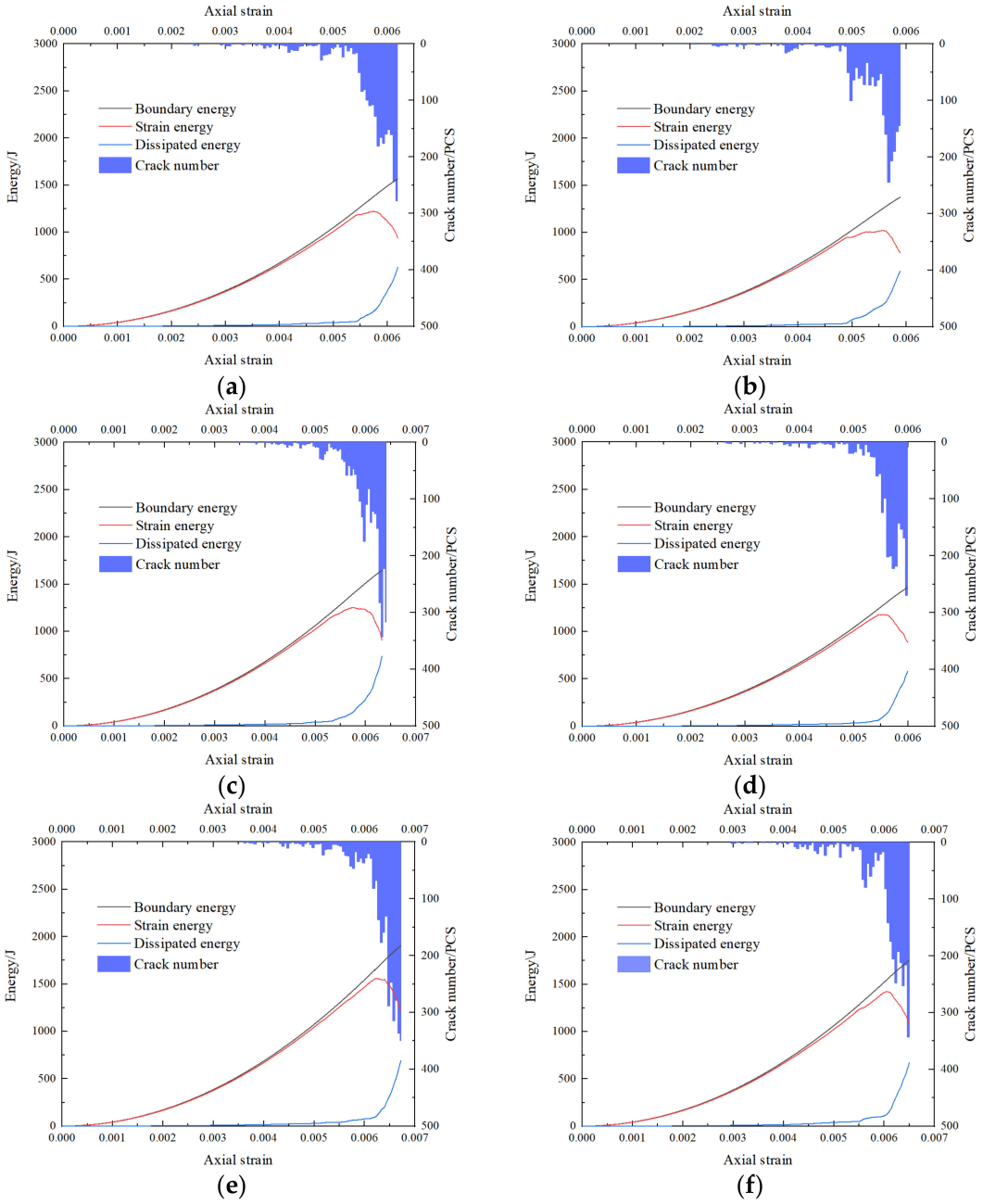

Figure 9. Curves of energy and crack number evolution of flawed samples: (**a**) E30; (**b**) F30; (**c**) E45; (**d**) F45; (**e**) E60, and (**f**) F60.

5. Discussion

PFC2D was utilized to simulate the uniaxial compression test of samples containing two pre-existing flaws. The strength and strain energy of the sample increased with the increase in the flaw angle. The existence of flaws of unequal length in the sample weakened the performance (strength, strain energy, etc.) of the sample.

The peak strength and crack initiation strength were obtained based on the test results. The ratios of the crack initiation strength, which are normalized by respective peak strength, are plotted against the flaw angle in Figure 10. The strength ratios in both samples with flaws of equal length (Sample E) and samples with flaws of unequal length (Sample F) increase with the increase in the flaw angle. The highest strength ratio is reached at $\theta = 60°$, but it is still less than 1. It shows that further loading is required after the appearance of cracks for the sample to fail. The ratios of crack initiation strength of Sample E are higher than those of Sample F. The main factor is that the flaws of unequal length in the sample weaken the performance of the sample.

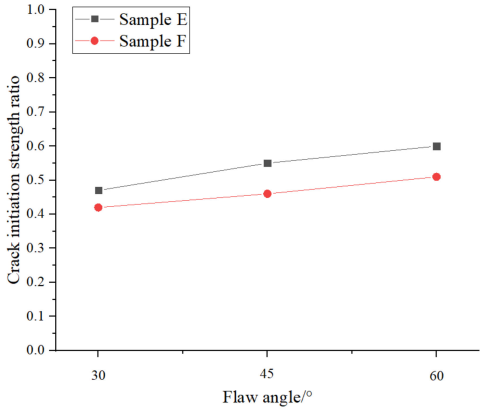

Figure 10. Crack-initiation strength normalized by the respective sample strength versus the flaw angle.

To further analyze the energy characteristics of samples with different flaw angles and types, the boundary energy U, strain energy U^e, and dissipated energy U^d of samples with different flaw angles under peak strength are shown in Figure 11. There is an obvious relationship between the energy and the flaw angle of the sample. U and U^e increase with the increase in flaw angle, and the curves are approximately linear. Most of the energy is still stored in the form of strain energy. The results are consistent with those of Jin et al. [19] and Li et al. [20]. As suggested in other numerical studies, the energy and dissipated energy U^d used in crack initiation and coalescence and the friction between particle and particle are inferior in the boundary energy U. The boundary energy U and strain energy U^e of Sample F are smaller than those of Sample E. The energy storage limit of the samples with flaws of unequal length is reduced.

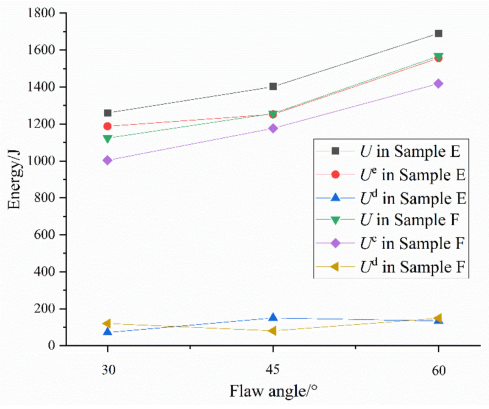

Figure 11. Energy variation of samples with different flaw angles.

6. Conclusions

(1) The crack-initiation strength and peak strength of the sample increase with the increase in the flaw angle. When the flaw angle is small, the sample shows plastic deformation during uniaxial compression. For larger flaw angles, the sample shows elastic-brittle properties, whose storage energy is larger.

(2) The existence of flaws of unequal length in the sample reduces the stability of the sample. The crack-initiation strength and peak strength of the sample with flaws of unequal length were 18.76% and 6.15% smaller than those of the sample with flaws of equal length, respectively.

(3) The energy-storage limit of the samples with flaws of unequal length is reduced to a certain extent. The strain energy reaches an extreme value at the peak strength, whose growth rate first increases with the strain and then gradually decreases. The strain energy is accumulated in the pre-peak region and released in the post-peak region. The dissipated energy is concave upward with the strain, and the growth rate increases gradually.

Author Contributions: Conceptualization, C.H. and Y.Z.; methodology, Q.L. and X.Y.; software, Q.L. and P.L.; validation, Q.L. and G.Y.; investigation, Q.L.; data curation, Q.L.; writing—original draft preparation, Q.L.; writing—review and editing, Q.L. and P.L. All authors have read and agreed to the published version of the manuscript.

Funding: This research was funded by the National Natural Science Foundation of China (grant number 52074123), the Natural Science Foundation of Hebei Province, China (grant number E2021209148, E2022209143), and the Science and Technology Project of Hebei Education Department (grant number QN2021111).

Institutional Review Board Statement: Not applicable.

Informed Consent Statement: Not applicable.

Data Availability Statement: The data presented in this study are available on request from the corresponding author.

Conflicts of Interest: The authors declare no conflict of interest.

References

1. Prudencio, M.; Jan, M. Strength and failure modes of rock mass models with non-persistent joints. *Int. J. Rock Mech. Min. Sci.* **2007**, *44*, 890–902. [CrossRef]
2. Feng, F.; Chen, S.; Wang, Y.; Huang, W.; Han, Z. Cracking mechanism and strength criteria evaluation of granite affected by intermediate principal stresses subjected to unloading stress state. *Int. J. Rock Mech. Min. Sci.* **2021**, *143*, 104783. [CrossRef]
3. Bobet, A.; Einstein, H. Fracture coalescence in rock-type material under uniaxial and biaxial compression. *Int. J. Rock Mech. Min. Sci.* **1998**, *35*, 863–888. [CrossRef]
4. Park, C.; Bobet, A. Crack coalescence in specimens with open and closed flaws: A comparison. *Int. J. Rock Mech. Min. Sci.* **2009**, *46*, 819–829. [CrossRef]
5. Park, C.; Bobet, A. Crack initiation, propagation and coalescence from frictional flaws in uniaxial compression. *Eng. Fract. Mech.* **2010**, *77*, 2727–2748. [CrossRef]
6. Wong, R.; Chau, K. Crack coalescence in a rock-like material containing two cracks. *Int. J. Rock Mech. Min. Sci.* **1998**, *35*, 147–164. [CrossRef]
7. Wong, L.; Einstein, H. Crack coalescence in molded gypsum and Carrara marble: Part 1. macroscopic observations and interpretation. *Rock Mech. Rock Eng.* **2009**, *42*, 475–511. [CrossRef]
8. Morgan, S.; Johnson, C.; Einstein, H. Cracking processes in Barre granite: Fracture process zones and crack coalescence. *Int. J. Fract.* **2013**, *180*, 177–204. [CrossRef]
9. Lee, H.; Jeon, S. An experimental and numerical study of fracture coalescence in pre-cracked specimens under uniaxial compression. *Int. J. Solids Struct.* **2011**, *48*, 979–999. [CrossRef]
10. Yang, S.; Liu, X.; Jing, H. Experimental investigation on fracture coalescence behavior of red sandstone containing two unparallel fissures under uniaxial compression. *Int. J. Rock Mech. Min. Sci.* **2013**, *63*, 82–92. [CrossRef]
11. Afolagboye, L.; He, J.; Wang, S. Experimental study on cracking behaviour of moulded gypsum containing two non-parallel overlapping flaws under uniaxial compression. *Acta Mech. Sin.* **2017**, *33*, 394–405. [CrossRef]

12. Yang, S.; Tian, W.; Huang, Y.; Ranjith, P.; Ju, Y. An experimental and numerical study on cracking behavior of brittle sandstone containing two non-coplanar fissures under uniaxial compression. *Rock Mech. Rock Eng.* **2016**, *49*, 1497–1515. [CrossRef]
13. Huang, Y.; Yang, S.; Tian, W.; Zeng, W.; Yu, L. An experimental study on fracture mechanical behavior of rock-like materials containing two unparallel fissures under uniaxial compression. *Acta Mech. Sin.* **2016**, *32*, 442–455. [CrossRef]
14. Saadat, M.; Taheri, A. A numerical approach to investigate the effects of rock texture on the damage and crack propagation of a pre-cracked granite. *Comput. Geotech.* **2019**, *111*, 89–111. [CrossRef]
15. Abdollahipour, A.; Marji, M.F. Analyses of inclined cracks neighboring two iso-path cracks in rock-like specimens under compression. *Geotech. Geol. Eng.* **2017**, *35*, 169–181. [CrossRef]
16. Tang, L.; Song, Y. Particle flow simulation of macro- and meso-mechanical properties of uniaxially compressed rock-like specimens with non-coplanar overlapping flaws. *Chin. J. Rock Mech. Eng.* **2019**, *38*, 2161–2171.
17. Chen, S.; Feng, F.; Wang, Y.; Li, D.; Huang, W.; Zhao, X.; Jiang, N. Tunnel failure in hard rock with multiple weak planes due to excavation unloading of in-situ stress. *J. Cent. South Univ.* **2020**, *27*, 2864–2882. [CrossRef]
18. Huang, D.; Cen, D. Mechanical responses and energy dissipation mechanism of rock specimen with a single fissure under static and dynamic uniaxial compression using particle flow code simulations. *Chin. J. Rock Mech. Eng.* **2013**, *32*, 1926–1936.
19. Jin, J.; Cao, P.; Chen, Y.; Pu, C.; Mao, D.; Fan, X. Influence of single flaw on the failure process and energy mechanics of rock-like material. *Comput. Geotech.* **2017**, *86*, 150–162. [CrossRef]
20. Li, X.; Yao, Z.; Liu, X.; Huang, X. Energy evolution and damage mechanism of fractured sandstone with different angles. *Energies* **2022**, *15*, 1518. [CrossRef]
21. Wang, J.; Chen, Z.; Zhang, L. Unloading-induced crack propagation of two collinear unequal length flaws in brittle rocks. *Geofluids* **2020**, *2020*, 1–18. [CrossRef]
22. Craciun, E.; Soós, E. Interaction of two unequal cracks in a prestressed fiber reinforced composite. *Int. J. Fract.* **1998**, *94*, 137–159.
23. Fan, Y.; Zhu, Z.; Kang, J.; Fu, Y. The mutual effects between two unequal collinear cracks under compression. *Math. Mech. Solids* **2017**, *22*, 1205–1218. [CrossRef]
24. Yu, B.; Xi, J.; Chen, Z.; Zhang, L. Interaction analysis of collinear two cracks with unequal length under uniaxial traction. *Math. Probl. Eng.* **2019**, *2019*, 1–15. [CrossRef]
25. Xie, H.; Ju, Y.; Li, L. Criteria for strength and structural failure of rocks based on energy dissipation and energy release principles. *Chin. J. Rock Mech. Eng.* **2005**, *24*, 3003–3010.
26. *Manual of Particle Flow Code in 2-Dimension*, version 5.0; Itasca Consulting Group Inc.: Minneapolis, MN, USA, 2014.
27. Cho, N.; Martin, C.; Sego, D. A clumped particle model for rock. *Int. J. Rock Mech. Min. Sci.* **2007**, *44*, 997–1010.
28. Potyondy, D.; Cundll, P. A bonded-particle model for rock. *Int. J. Rock Mech. Min. Sci.* **2004**, *41*, 1329–1364. [CrossRef]
29. Zhang, X.; Wong, L. Cracking processes in rock-like material containing a single flaw under uniaxial compression: A numerical study based on parallel bonded-particle model approach. *Rock Mech. Rock Eng.* **2012**, *45*, 711–737. [CrossRef]
30. Li, Q.; Li, Z.; Xu, X. Experimental study for the effect of fillings on properties of brittle rock containing two parallel flaws. *Geotech. Geol. Eng.* **2020**, *38*, 3643–3651. [CrossRef]